PHYSICAL REVIEW FLUIDS **11**, 064303 (2026)

Editors' Suggestion

Pattern formation in rectilinear flows of noncolloidal suspensions

Parham Poureslami
Department of Mechanical Engineering, University of Minnesota, Minneapolis 55455, Minnesota, USA and St. Anthony Falls Laboratory, University of Minnesota, Minneapolis 55414, Minnesota, USA

Ranit Mukherjee
Department of Mechanical Engineering, University of Minnesota, Minneapolis 55455, Minnesota, USA

Sungyon Lee [*]
Department of Mechanical Engineering, University of Minnesota, Minneapolis 55455, Minnesota, USA and St. Anthony Falls Laboratory, University of Minnesota, Minneapolis 55414, Minnesota, USA

(Received 23 January 2026; accepted 29 April 2026; published 10 June 2026)

The displacement of air by a noncolloidal particulate suspension between two parallel plates can trigger interfacial instabilities and two seemingly intertwined patterns: deformation of the fluid-fluid interface and dense particle clusters within the suspension, hereafter referred to as plumes. While prior studies have primarily examined the onset and source of this instability, the emergence and coupling of these patterns remain unresolved. Notably, existing investigations have been limited to radial geometries, where continuous outward expansion of the interface weakens plume-plume interactions. Here, we experimentally displace air with an oil suspension in a rectangular Hele-Shaw cell. Confinement within a constant-width channel amplifies interactions between neighboring plumes, giving rise to previously unreported regimes of pattern formation, including plume merging and plume shedding. Image analysis reveals strong coupling between interfacial deformation and plumes and characterizes the interaction between adjacent plumes. Employing the suspension balance model, we demonstrate how net particle flux toward the interface drives particle accumulation and establishes the conditions for pattern formation. Namely, particle clustering at the interface locally slows the advancing interface and produces concave plume tips that become preferential sites for plume initiation. In addition, we develop a simple scaling for the size of the interfacial deformation based on the interplay between upstream pressure, interface concentration, and plume concentration.

DOI: 10.1103/tgvb-bh1n

I. INTRODUCTION

Patterns emerge spontaneously along the unstable fluid-fluid interface in nonequilibrium systems [1,2]. Understanding how these patterns develop and evolve is essential for advancing both fundamental science and practical applications, including oil recovery [3], carbon sequestration [4], coating processes [5–7], additive manufacturing [8], and targeted drug delivery [9]. Of particular interest is pattern formation in particle-laden flows [10–15], especially when one fluid invades another immiscible one in a confined channel [16]. This invasion mechanism frequently triggers interfacial instabilities, leading to striking patterns with rich underlying physics [17–20].

[*]Contact author: sungyon@umn.edu

In such a scenario, particles contribute to pattern formation through disparate mechanisms. First, the granular nature of particles alters the morphology of emerging patterns by introducing interparticle friction. In these experiments, a low-viscosity fluid (i.e., air) displaces a bed of heavy particles saturated with a more viscous defending fluid inside a Hele-Shaw cell [17,21–24]. As air is injected, the particles progressively accumulate near the advancing interface, creating a jammed front that exerts a frictional force. The interplay between this force and capillary and viscous forces dictates the resulting pattern dynamics. In the absence of particles, owing to a destabilizing viscosity ratio between the invading and defending phases, this viscous multiphase flow reduces to the well-known viscous fingering patterns, where fingerlike protrusions advance into the defending fluid [25–27].

Alternatively, suspended particles can destabilize fluid-fluid interfaces when sheared between two parallel plates. Notably, neutrally buoyant noncolloidal particles suspended in a viscous fluid can induce viscous fingering during air displacement inside a Hele-Shaw cell, despite a stabilizing viscosity contrast between the invading and defending fluids [28,29]. Commonly termed "particle-induced viscous fingering" (PIVF), this counterintuitive instability arises solely due to noncolloidal particles, as the interface would otherwise remain stable. The fundamental mechanism behind PIVF is shear-induced migration, which drives particles toward low-shear regions inside the gap, or the channel centerline where the flow is faster [30]. As a result, particles move faster than the average flow velocity and accumulate on the advancing interface in a quasi-self-similar manner, as mathematically rationalized in [31]. More recent studies [32–35] systematically demonstrated the dependence of PIVF on the particle volume fraction (ϕ_0) and channel confinement (b/d), defined as the ratio of Hele-Shaw gap thickness b to the particle diameter d.

Across all parameter regimes, particle-induced viscous fingering leads to two concurrent patterns: (i) deformation of the suspension-air interface and (ii) formation of dense, streamwise-advected particle clusters oriented normal to the interface. We refer to these particle clusters as "particle plumes," or plumes for brevity. Despite their apparent coupling, the interplay between interfacial deformation and these plumes has not been explored. Moreover, previous studies have focused exclusively on radial flow configurations, where the inherent flow field expansion augments the plume spacing, thereby suppressing plume-plume interactions. These observations prompt several open questions: Does confining the suspension flow to a rectangular channel of constant width enhance plume interactions? How do plumes form? And how does particle clustering influence interface deformation?

To address these questions, we experimentally investigate the formation and evolution of patterns in PIVF, as a suspension of silicone oil and noncolloidal particles invades air in a rectangular Hele-Shaw cell. Following the experimental method detailed in Sec. II, we observe four distinct pattern formation regimes in Sec. III A via changes in ϕ_0, including two newly identified regimes that are unique to the rectilinear flow configuration. Subsequently, in Sec. III B, we quantify emerging patterns, focusing on interface deformation, plume dynamics, and their potential coupling. In Sec. IV, we build on the particle accumulation rationalized via suspension balance model [36,37] and elucidate the mechanism of plume formation and their sustained growth. Finally, we conclude the paper with a summary in Sec. V.

II. METHODS

A. Setup

Experiments are conducted by injecting a mixture of silicone oil and rhodamine B polyethylene particles into a horizontally oriented rectangular Hele-Shaw cell initially filled with quiescent air [Fig. 1(a)]. The quasineutrally buoyant, noncolloidal particles (Cospheric, diameter $d =$ 125–150 μm, density $\rho_\mathrm{p} = 980\,\mathrm{kg/m^3}$) are spherical and remain suspended in oil (Sigma-Aldrich, $\mu_1 = 0.048$ Pa s, density $\rho_1 = 963$ kg/m^3, interfacial tension $\gamma = 21$ mN/m) over the timescale of the experiments. The cell consists of two rigid glass plates (610 mm × 310 mm, 10 mm thickness),

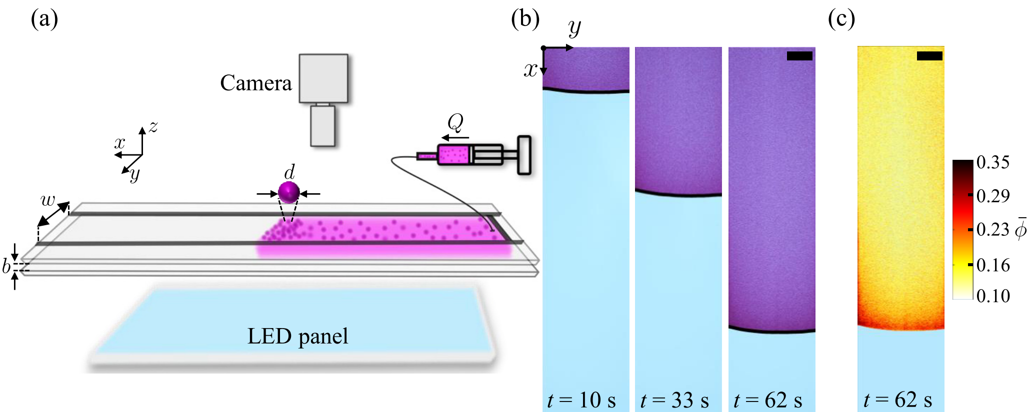

FIG. 1. (a) Schematic diagram of the experimental setup. (b) Snapshots of the suspension invading air at $\phi_0 = 0.15$, representing the stable regime with negligible interfacial deformation. The solid black lines reveal the suspension-air interface identified by edge detection. (c) Corresponding depth-averaged particle concentration ($\bar{\phi}$) field at $t = 62$ s, indicating the particle accumulation near the advancing interface. Scale bars in (b) and (c) denote 2 cm.

separated by steel shims (McMaster) with a uniform thickness $b = 1.52$ mm. An injection hole with a diameter of 5.3 mm is drilled into the top plate of the cell, with its center located 48 mm from the rightmost edge. The suspension flow passage is sealed and laterally confined to a width of $w = 70$ mm using high-density foam tapes, marginally thicker than the gap spacing. Upon clamping the glass plates, the foam compresses to match the final gap thickness. To prepare the suspension, particles are added to silicone oil to achieve the desired initial volume fraction ($0.15 \leqslant \phi_0 \leqslant 0.40$), and the mixture is gently shaken inside the syringe to ensure homogeneous particle distribution. The syringe is then held vertically, allowing trapped air bubbles to rise and escape. The bubble-free suspension is subsequently injected into the cell at a constant flow rate ($Q = 25$ ml/min) using a syringe pump (New Era) through a short vinyl tube with the inner diameter of 4.7 mm. Mounted above the cell, a CMOS camera (Nikon D500) equipped with a Nikkor 16–80 mm f/2.8 lens records the suspension invasion process at a shooting rate of 24 fps and a resolution of 3840 pixels × 2160 pixels, with each pixel corresponding to approximately 85.4 μm. The imaging window begins 53 mm downstream from the inlet and spans 328 mm along the x direction, enabling the visualization of pattern development beyond the initial stable front. Illumination is provided by a 40 W LED panel light (603 mm × 603 mm) placed beneath the cell for even lighting.

Although additional experiments are carried out by systematically varying the volume flow rate, channel width, and silicone oil viscosity, their influence on the regimes of pattern formation is found to be negligible compared to that of the particle volume fraction (see Appendix A). Accordingly, this study centers on the role of volume fraction as the primary governing parameter. All experiments are conducted in the low Reynolds number [$\mathrm{Re} = \rho_1 U b/\mu_1 \sim O(10^{-1})$] and low capillary number [$\mathrm{Ca} = \mu_1 U/\gamma \sim O(10^{-3})$] regimes, while the large Péclet number [i.e., $\mathrm{Pe} \sim O(10^{10})$] ensures that Brownian motion of the particles can be overlooked. Here, $U \approx 3.89$ mm/s is the average interface velocity, obtained by tracking the mean interface position over time. Figure 1(b) shows a typical experiment at $\phi_0 = 0.15$, where $t = 0$ marks the moment the suspension first enters the imaging window. For $\phi_0 \leqslant 0.15$, the interface exhibits negligible deformation, and no particle clustering is observed, resulting in the stable regime (see Supplemental Material [38], movie S1).

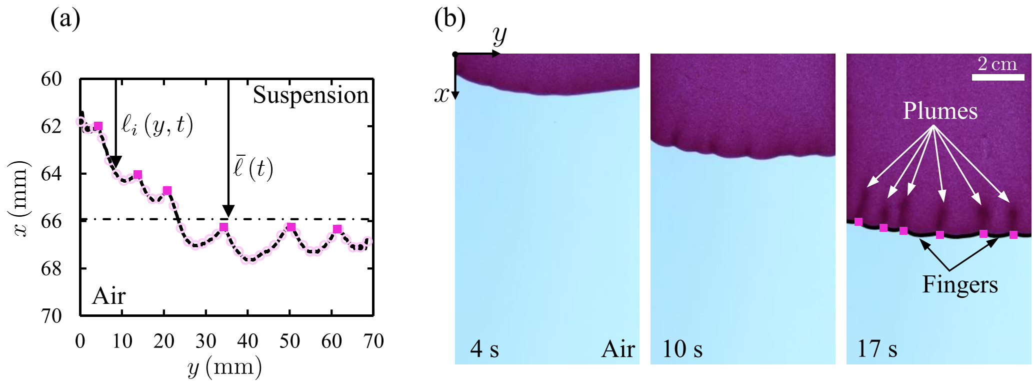

FIG. 2. (a) Reconstructed interface (solid black line) obtained via inverse FFT at $t = 17$ s, corresponding to the experiment shown in (b). Pink circles denote the edge-detected interface, solid squares indicate plume tips, and the dash-dotted line marks the mean interface position $\bar{\ell}(t)$. To enhance visual clarity, edge-detected data points are subsampled at a 1:20 ratio. The x coordinate increases in the downward direction. (b) A typical example of pattern formation and plume emergence in a representative experiment at $\phi_0 = 0.25$. Illustrated at $t = 17$ s, plume tips (solid squares) are located on the local minima of the interface between two consecutive fingers, which are extracted from the reconstructed interface. This consistent feature holds in all experiments.

B. Data analysis

Image postprocessing is performed using an in-house MATLAB code. Following background subtraction, the suspension-air interface is detected using the Canny edge detection method, which identifies edges by locating local maxima of the intensity gradient in the grayscale image [39], as illustrated in Fig. 1(b). From these processed images, we obtain the depth-averaged concentration field $\bar{\phi}$ [Fig. 1(c)] by using an empirical relation between image intensity and $\bar{\phi}$ that is established through independent calibration experiments (see Appendix B).

In addition to extracting $\bar{\phi}$, we quantify the interface deformation by measuring the standard deviation of the interface position:

$$\sigma(t) = \sqrt{\frac{\sum_{i=1}^{N}(\ell_i - \bar{\ell})^2}{N}}, \tag{1}$$

where $\ell_i(y,t)$ and $\bar{\ell}(t)$ are the local and mean interface positions, respectively, as illustrated in Fig. 2(a). In addition, N is the number of detected edge points along the interface. To reconstruct a smooth interface from the discrete set of points, we apply the fast Fourier transform (FFT) to the edge-detected interface profile and filter out high-frequency components above a specified threshold. Then, we compute the inverse FFT, which yields a smoother interface shape [Fig. 2(a)]. This allows us to obtain the localized geometrical information of the evolving interface. To avoid artifacts introduced by the inverse FFT near the image boundaries, the lateral 1% of the interface on both the left and right sides is excluded from the analysis.

III. EXPERIMENTS

A. Regimes of pattern formation

As discussed earlier, when $\phi_0 \leqslant 0.15$, the interface remains stable to PIVF over the length scale of the experiments [see Fig. 1(b)]. Then, as ϕ_0 is increased above $\phi_0 = 0.15$, instabilities emerge with the concurrent appearance of interfacial fingers and particle clusters, or "plumes," as shown in Fig. 2(b). We identify four distinct regimes of pattern formation based on the observed plume dynamics: stable (see Sec. II A), isolated plumes, merging plumes, and plume shedding. The latter

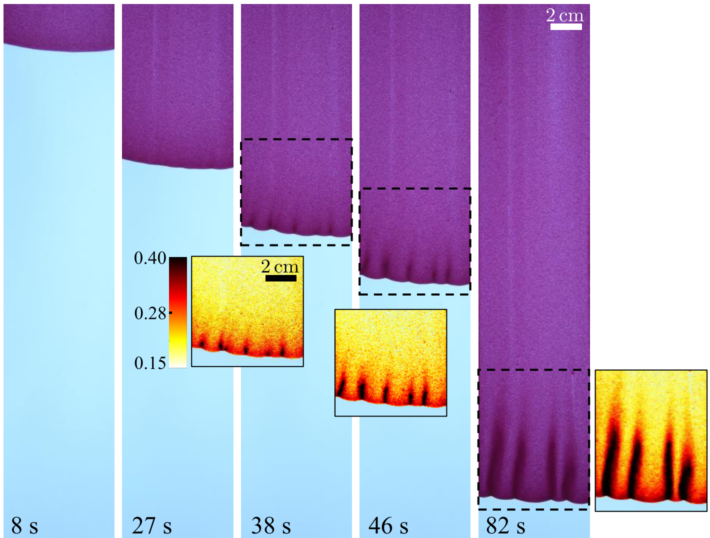

FIG. 3. Time sequential images of isolated plumes regime at $\phi_0 = 0.20$. The insets depict the depth-averaged particle concentration ($\bar{\phi}$) of the regions highlighted by the dashed rectangles.

three regimes are illustrated in Figs. 3–5, respectively, where insets display the depth-averaged concentration field ($\bar{\phi}$) within the region indicated by the dashed rectangle. For clarity, the color map is recalibrated in each regime to accentuate the detailed structure inside the suspension.

As shown in Fig. 3, the isolated plumes regime arises at $\phi_0 = 0.20$ (see Supplemental Material [38], movie S2). During the early stages, the advancing suspension front is stable. However, particle accumulation at the interface eventually initiates plume formation, accompanied by subtle yet discernible interfacial deformation ($t = 38$ s). The subsequent axial growth of these plumes

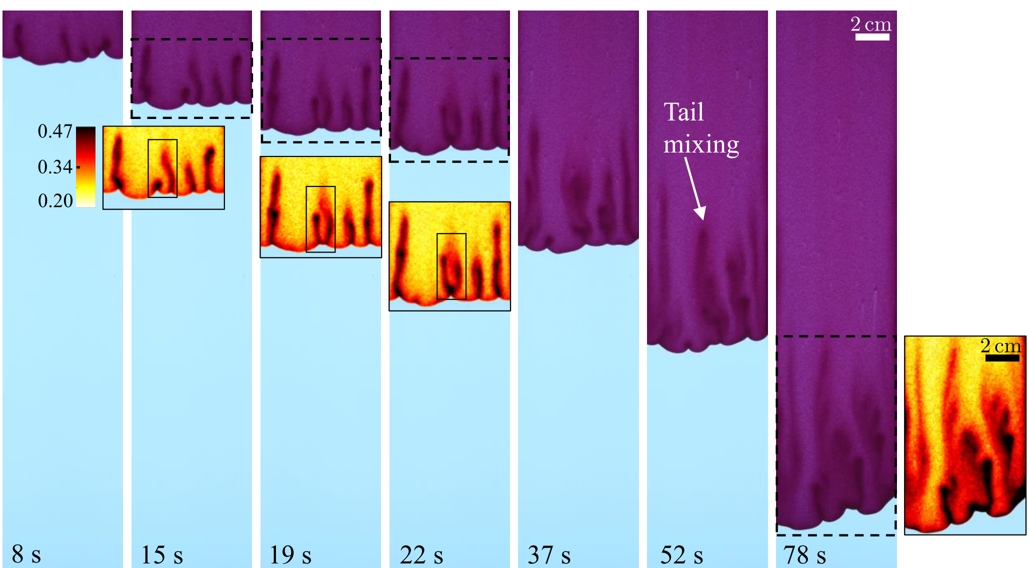

FIG. 4. Time sequential images of merging plumes regime at $\phi_0 = 0.30$. The merging process of neighboring plumes is depicted by the solid rectangles in the inset, spanning from $t = 15$ to 22 s.

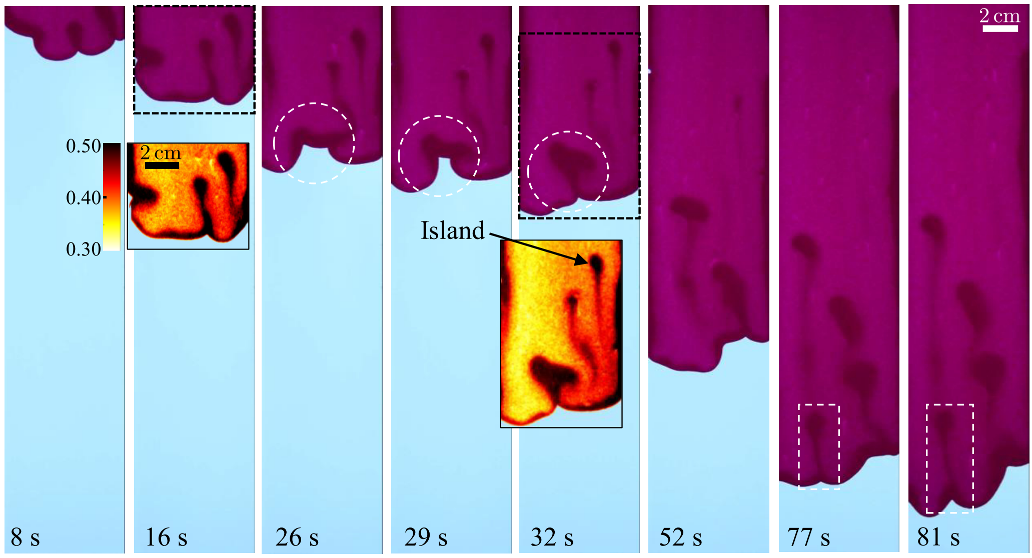

FIG. 5. Time sequential images of plume shedding regime at $\phi_0 = 0.40$. The detachment of plumes from the advancing interface occurs via two pathways. In the first mechanism, the edges of a thick particle band coalesce, leaving an "island" behind, as highlighted between 26 and 32 s by the white dashed circles. In the second mechanism, shedding occurs through the independent growth of individual plumes without interaction with their neighbors, as highlighted between 77 and 81 s by the white dashed rectangles. Image brightness and contrast have been adjusted to enhance visual clarity.

over time is evident, with their average length reaching approximately 25.0 mm within 30 s of emergence. In this regime, plumes predominantly remain isolated and evolve independently with negligible influence on their neighbors. In view of this inherent isolation, the plume behavior in this regime resembles previous observations in radial source flows, where flow expansion inhibits plume interaction and coalescence [40]. Notably, a plume tip, or the downstream end of a plume that meets the interface, consistently coincides with the local minimum of the interface, as clearly identified from the reconstructed interface profiles [Fig. 2(a)]. This observation holds across all instability regimes and will be further discussed in Sec. IV B.

When ϕ_0 is increased to 0.30, Fig. 4 illustrates that the plumes begin to frequently interact with their neighbors, as they grow in the flow direction (see Supplemental Material [38], movie S3). This new phenomenon arises from the lateral confinement of the flow passage, where the presence of side walls restricts transverse expansion and promotes plume-plume interactions. During interaction, adjacent plumes approach one another, and their tips eventually coalesce, or merge. A clear example of a merging event is highlighted in the inset from $t = 15$ to 22 s. Owing to this dominant behavior, we refer to this regime as the merging plumes regime. However, we note that not all adjacent plumes undergo this process. Following coalescence, the tails of the merged plumes appear to "diffuse" into the background flow, leading to particle mixing unobserved in the isolated plumes regime (see Fig. 4 at 52 and 78 s). In addition to enhanced mixing, the interfacial deformation is also more pronounced than in the former regime.

Despite their differences, the transition from isolated plumes to merging plumes regimes tends to be gradual, rather than abrupt. For instance, merging events can occasionally be observed even in the isolated plumes regime, provided the initial spacing between plume tips is sufficiently small (on the order of 1 mm). When $0.20 < \phi_0 < 0.30$, the resulting patterns inherit features from both the isolated plume and merging plume regimes: while the number of plumes and the extent of interfacial deformation resemble those in the latter, the plumes largely evolve independently, akin to the former.

Accordingly, the experiments carried out within this range are classified as the transition region. Finally, plumes remain attached to the interface while being advected downstream in all regimes encompassing isolated and merging plumes.

As displayed in Fig. 5, further increasing the particle volume fraction ($\phi_0 \geqslant 0.35$) leads to a surprising regime in which plumes no longer remain attached to the interface (see Supplemental Material [38], movie S4). Instead, the newly formed plumes intermittently detach from the advancing interface, bringing about dense particle islands within the suspension. These islands are then advected downstream by the background flow, one of which is displayed at $t = 32$ s. In view of this intermittent detachment, we refer to this regime as plume shedding, as it is reminiscent of vortex shedding from a bluff body in shear flow [41]. A similar plume detachment has also been observed in different contexts that involve nonhydrodynamic effects. They range from cell swarms due to signaling gradients [42] to colloid precipitation at a miscible fluid interface [43] governed by the interplay between chemical reactions and hydrodynamics. Going back to the present experiments, the instability develops immediately upon the suspension entering the cell given the high initial particle concentration and exhibits the most pronounced interfacial deformation. Furthermore, plumes themselves do not necessarily resemble thin clusters of particles that grow normal to the interface; instead, they may be a thick band of particles on the interface that preferentially move slower than the advancing front.

Interestingly, the close examination of the shedding event reveals its close connection to plume coalescence. As shown in Fig. 5, around $t = 26$ s, a thick band of particles on the interface lags behind the rest of the advancing interface. Then, the edges of the band are drawn together and ultimately collapse onto each other, or “coalesce,” by $t = 32$ s, which leaves an island of particles behind in the process. If one thinks of the edges of the particle band as individual plumes from the previous regime, plume shedding is analogous to plume interaction. In this sense, plume shedding frequently arises as a consequence of plume-plume interaction, suggesting that the merging and shedding regimes likely lie on a continuum, with the transition from one to the next set by increasing particle accumulation between the plumes as ϕ_0 increases. However, unlike in the merging plumes regime, where the merged tails blend into the background suspension, the coalescence here is followed by the detachment of the plume tails, generating the islands. In addition, plume shedding does not strictly require interaction between neighboring plumes: individual plumes may grow independently and still undergo tail detachment, as highlighted in Fig. 5 between $t = 77$ and 81 s.

Looking at all the regimes together, Fig. 6(a) presents time-averaged instability wavelength $\bar{\lambda}$ as a function of ϕ_0. Here, $\bar{\lambda}$ is calculated as the temporal mean of the average distance between two consecutive plume tips at each instant. The plume shedding regime exhibits the largest $\bar{\lambda}$. Since $\bar{\lambda}$ varies inversely with the number of plumes n_p, this regime generally features the lowest n_p at any given time. Additionally, except for $\phi_0 = 0.40$, the wavelength and number of plumes do not alter significantly over time. This trend is further illustrated in Fig. 6(b), tracking the time variation of n_p at $\phi_0 = 0.30$. In general, a reduction in n_p occurs through two primary mechanisms: (i) merging of neighboring plumes, discussed above. (ii) Over the course of evolution, plumes, especially those close to the side walls, are drawn laterally to the side walls and eventually collide with the boundaries. Upon colliding with the wall, plumes are annihilated, and the resulting particles deposit on the side wall. Hence, not all plumes persist over the entire duration of the experiment; some exhibit shorter lifespans, particularly those originating near the side walls. Importantly, as certain plumes dissipate, new plumes may emerge.

B. Quantitative examination of patterns

In this section, we quantify the interplay between interfacial deformation and particle concentration within the plumes [$\bar{\phi}_p(t)$], elucidating how local variation in suspension concentration modulates the interface morphology. Figure 7(a) examines the time variation of normalized interfacial deformation σ/b, obtained from Eq. (1), for varying ϕ_0. The peaks and valleys prominently featured in the plume shedding regime are attributed to shedding events. The interfacial deformation

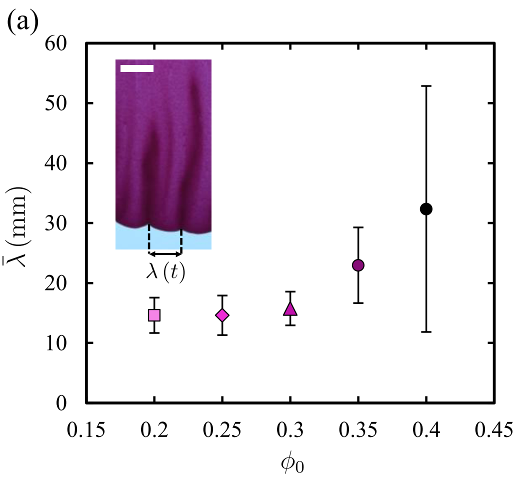

FIG. 6. (a) Time-averaged instability wavelength ($\bar{\lambda}$) as a function of ϕ_0 for isolated plumes (square), transition (diamond), merging plumes (triangle), and plume shedding (circle) regimes. Error bars represent the standard deviation of the measurements. The inset defines the instantaneous wavelength $\lambda(t)$, determined as the mean distance between two consecutive plume tips at each moment. (b) Number of plumes (n_p) versus time for $\phi_0 = 0.30$, determined by tracking the number of distinct plume tips over time. Changes in n_p occur due to two main phenomena: (i) merging, which accounts for the decrease in n_p from 43 to 48 s, where two simultaneous merging events take place, highlighted by white and black dashed rectangles in the upper inset; and (ii) plume collision with the side walls, explaining the reduction in n_p from 58 to 64 s, as indicated by black dashed rectangles in the lower inset. Scale bars correspond to 2 cm.

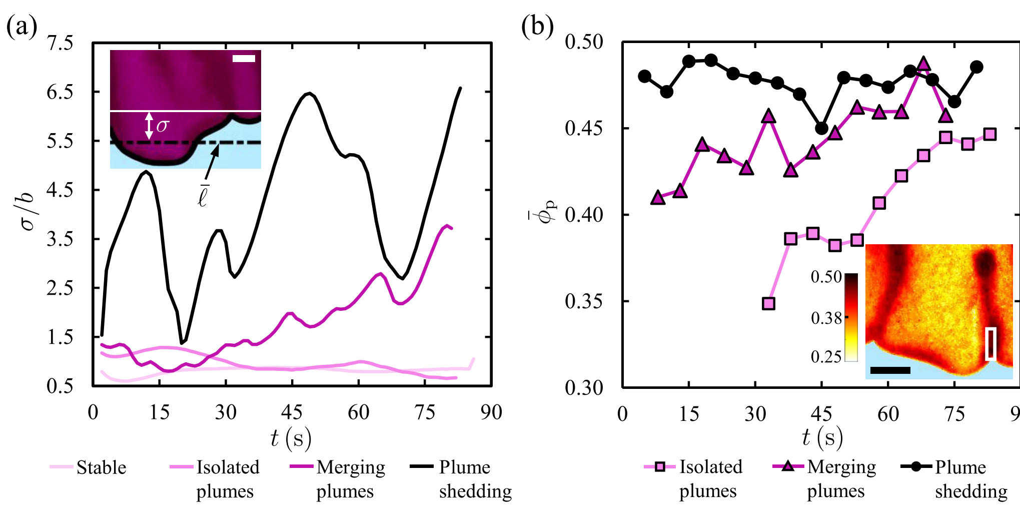

FIG. 7. Temporal evolution of dimensionless interfacial deformation (σ/b) and plume concentration ($\bar{\phi}_p$) for distinct PIVF regimes. (a) σ/b vs t; the inset highlights the parameters detailed in Sec. II B: the black solid line traces the suspension-air interface, the dash-dotted line indicates the mean interface position ($\bar{\ell}$), and the white solid line marks one standard deviation (σ) from the mean. (b) $\bar{\phi}_p$ vs t; the inset shows a representative concentration map, in which the white rectangle outlines the region used to determine $\bar{\phi}_p$. From bottom to top, the curves correspond to stable ($\phi_0 = 0.15$), isolated plumes ($\phi_0 = 0.20$), merging plumes ($\phi_0 = 0.30$), and plume shedding ($\phi_0 = 0.40$) regimes, while (b) includes only the latter three. Scale bars represent 1 cm.

first increases as the edges of the particle band are drawn towards each other. Once they merge, the interface relaxes, reducing σ. By contrast, the degree of deformation in the isolated plume regime is comparable to that in the stable regime, and almost an order of magnitude lower than that of the shedding regime. Finally, σ in the merging regime falls between the two extrema and exhibits some fluctuations related to the merging events.

To determine $\bar{\phi}_\mathrm{p}(t)$, a rectangular region of 1.3 mm in width and 6.0 mm in height is constructed above each plume tip [see the inset of Fig. 7(b)] such that the tip is located at the center of the bottom edge. The depth-averaged particle concentration within this region is defined as $\bar{\phi}_\mathrm{p}$. Measurements confirm that the concentration obtained from this representative region is insensitive to the rectangle size (see Appendix C), in light of the relatively uniform concentration from tip to tail. Since the particle concentration just near the air side sharply falls, the corresponding pixel values are excluded from the measurement through a threshold set approximately equal to ϕ_0 for each experiment. Moreover, plumes encompass a dense core and a surrounding shell of lower concentration, both of which are included in evaluating $\bar{\phi}_\mathrm{p}$.

Figure 7(b) presents the temporal evolution of plume concentration for distinct PIVF regimes, based on a representative plume selected from each case. The temporal trend of $\bar{\phi}_\mathrm{p}$ remains consistent across different plumes within the same regime, indicating that it is independent of the particular plume chosen (see Appendix D). Overall, $\bar{\phi}_\mathrm{p}$ increases with ϕ_0, although its dependence on time varies with the instability regime. In both the isolated and merging plumes regimes, $\bar{\phi}_\mathrm{p}$ gradually increases as the plumes evolve, with the isolated plumes regime exhibiting a more pronounced temporal growth. In contrast, $\bar{\phi}_\mathrm{p}$ remains relatively constant over time in the plume shedding regime, suggesting that plumes are fully "mature" when they first enter the cell in this high concentration regime.

We conjecture that the observed increase in interfacial deformation (σ/b) with ϕ_0 arises from enhanced particle clustering near the advancing interface. Simply put, dense clusters advance more slowly than the surrounding suspension due to their enhanced viscosity, which can be rationalized via the one-dimensional (1D) Darcy's law for simplicity [44]:

$$U = -\frac{b^2}{12\mu(\bar{\phi})}\frac{dp}{dx}, \tag{2}$$

where dp/dx is the pressure gradient along the x direction, and the effective suspension viscosity $\mu(\bar{\phi})$ is a function of the local concentration, given by Morris and Boulay [37]:

$$\frac{\mu(\bar{\phi})}{\mu_1} = 1 + 2.5\bar{\phi}\left(1-\frac{\bar{\phi}}{\phi_\mathrm{m}}\right)^{-1} + 0.1\left(\frac{\bar{\phi}}{\phi_\mathrm{m}}\right)^2\left(1-\frac{\bar{\phi}}{\phi_\mathrm{m}}\right)^{-2}. \tag{3}$$

Here, μ_1 and $\phi_\mathrm{m} = 0.62$ are the suspending oil viscosity and maximum packing fraction of spherical particles, respectively. Equation (3) is developed specifically for suspensions comprising rigid, non-colloidal particles in the limit of infinite Péclet number and vanishing Reynolds number [45]. As μ/μ_1 monotonically increases with concentration [i.e., inset of Fig. 8(b)], these clusters become more viscous with increasing ϕ_0, amplifying the velocity contrast along the interface. Consequently, the distance between plume tips (local minima of the interface) and interfacial fingers (local maxima) increases, leading to greater overall deformation.

This mechanism is illustrated schematically in Fig. 8(a): localized particle clusters at points 1 and 2 at time t_0 lag behind the surrounding interface and give rise to the emergence of concave tips at t_1, where air protrudes into the suspension. At these early times, the tip radius of curvature δ is large, and the pressure difference between the tip and adjacent flat interface is negligible, such that the pressure gradient must be approximately uniform along the interface. Under this condition, the ratio of the tip velocity to the interfacial velocity depends primarily on the local viscosity ratio and may be approximated by

$$\frac{u_\mathrm{t}}{U} \approx \frac{\mu(\bar{\phi}_\mathrm{int})}{\mu(\bar{\phi}_\mathrm{t})} < 1, \tag{4}$$

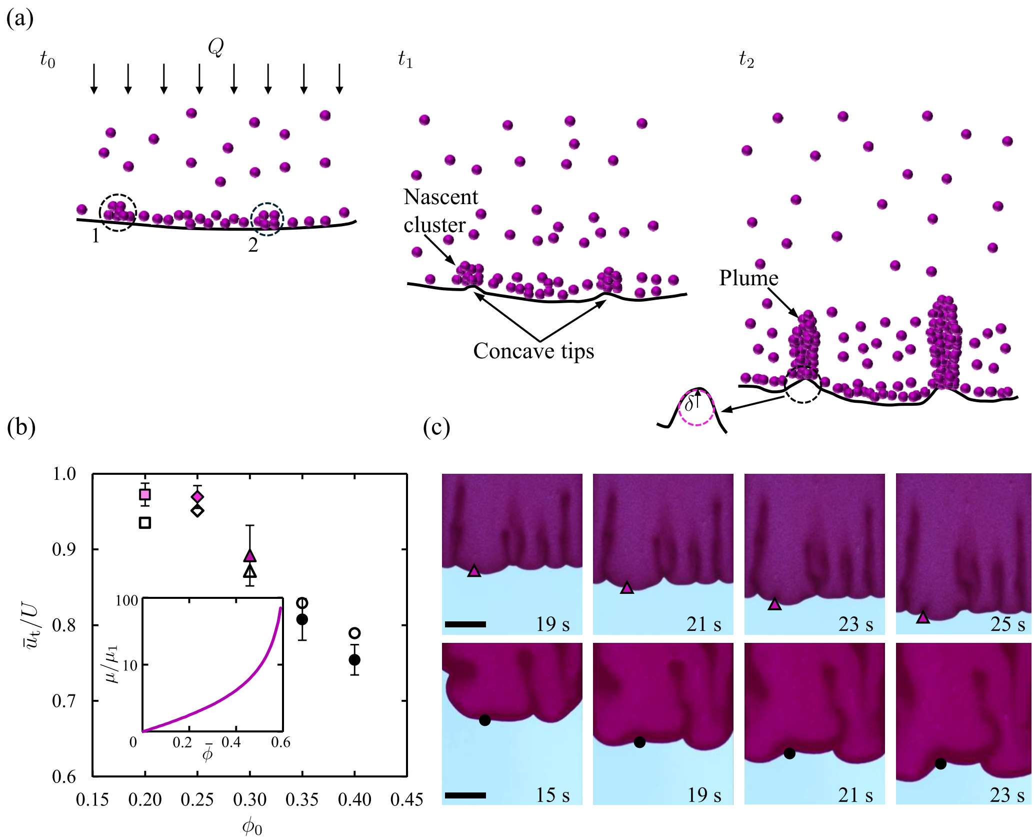

FIG. 8. (a) Schematic illustration of plume tip formation. Localized increases in particle concentration at points 1 and 2 at time t_0, caused by nascent clusters, lead these regions to lag behind the surrounding interface at time t_1. This delay produces concave tips that eventually act as initiation sites for plume growth at t_2. The inset shows the tip radius of curvature, δ. (b) Time-averaged tip velocity ($\bar{u}_t$), normalized by the interfacial velocity (U), as a function of ϕ_0. The experimental measurements (filled symbols) are compared with the 1D model (open symbols) derived from Darcy's law. Each data point represents the average across multiple tracked tips. The inset shows μ/μ_1 as a function of $\bar{\phi}$, based on the empirical expression by Morris and Boulay [37]. (c) Representative evolution of a tracked tip from initial clustering to plume formation at $\phi_0 = 0.30$ (top row) and $\phi_0 = 0.40$ (bottom row). For $\phi_0 = 0.40$, image brightness and contrast were adjusted for enhanced visual clarity. Scale bars represent 2 cm.

as dp/dx drops out of the expression. Here, $\mu\,(\bar{\phi}_t)$ is the viscosity of the clustering region immediately above the tip, and $\mu\,(\bar{\phi}_{int})$ is the mean suspension viscosity at the interface. The concentration $\bar{\phi}_t$ is determined using the same image-based method employed for plume concentration. Note that initially, the region above the tip is only weakly enriched, such that $\bar{\phi}_t < \bar{\phi}_p$. However, once the nascent cluster above the tip evolves into a plume, $\bar{\phi}_t$ becomes essentially identical to $\bar{\phi}_p$, as both correspond to the concentration of the same region in different stages of plume formation. From the experimental analysis depicted in the inset of Fig. 7(b), the mean concentration of particles at the interface ($\bar{\phi}_{int}$) is lower than $\bar{\phi}_t$, which indicates that ratio of u_t over U must be less than 1. We emphasize that Eq. (4) is intended to describe the mechanism of tip formation and is not meant to capture the subsequent evolution of mature plumes.

To validate the relationship between local interfacial velocity and particle concentration, we experimentally track the tip from the onset of clustering up to plume emergence. Figure 8(b) compares the experimentally measured time-averaged normalized tip velocity $\bar{u}_t/U$ with predictions from Eq. (4), while Fig. 8(c) presents one representative tracked tip under two different regimes. The simple model and experimental results are in close agreement, with an average relative error of only 3.1%. Importantly, $\bar{u}_t/U$ systematically decreases with increasing ϕ_0, which is consistent with μ/μ_1 in the inset of Fig. 8(b). As μ/μ_1 rises more steeply with increasing particle concentration, the viscosity contrast between particle clusters and the surrounding interface is expected to increase with ϕ_0, yielding a corresponding decrease in $\bar{u}_t/U$. In addition, this trend in μ/μ_1 explains why particle clusters that are observed even in the stable regime (i.e., $\phi_0 = 0.15$) do not develop into plumes within the experimental timescale, as the effective viscosity of clusters relative to the surrounding region is not high enough to generate concave tips. Going back to Fig. 8(b), the decrease in $\bar{u}_t/U$ aligns with the observed growth in interfacial deformation with ϕ_0, underscoring the tight coupling between interface deformation and plume formation. In the isolated plumes regime, $\bar{u}_t/U$ remains close to unity and yields only modest interfacial deformation, comparable to that in the stable regime. By contrast, in the merging plumes and plume shedding regimes, $\bar{u}_t/U$ is lower than 1, leading to a pronounced velocity contrast and substantially enhanced interfacial deformation. Finally, the evolution of "nucleating" particle clusters into mature plumes over time [e.g., t_2 in Fig. 8(a)] will be discussed in Sec. IV B.

C. Interaction of neighboring plumes

Having quantified the interrelated patterns, we now investigate the dynamics of neighboring plumes to elucidate the differences between interacting and noninteracting cases across all unstable regimes. As discussed earlier, two adjacent plumes that influence each other and eventually merge are referred to as interacting plumes, whereas the term noninteracting plumes is used otherwise. Notably, the highest number of interacting plumes occurs in the merging plumes regime, while noninteracting plumes are predominantly observed in the isolated plume regime.

To identify the most effective indicators of plume-plume interaction, several parameters were examined, among which two proved to be insightful: (i) the particle concentration between neighboring plumes ($\bar{\phi}_{ip}$) and (ii) the normalized local interfacial deformation between adjacent plumes (σ_{loc}/b). Figures 9(a) and 9(b) illustrate the time-averaged values of these two parameters as functions of ϕ_0, respectively, for both interacting and noninteracting plumes. As shown in the inset of Fig. 9(a), the interplume concentration, $\bar{\phi}_{ip}$, is measured within a rectangular region positioned between two neighboring plumes. The left and right edges of this region are offset by a distance $\mathcal{D}$ from the plume tips to exclude the plume cores from the measurement. The bottom edge is the first row in the image matrix where all pixels consist of air, while the top edge is set 6.0 mm above the plume tip with the smaller x position. The sensitivity analysis (Appendix C) confirms that $\bar{\phi}_{ip}$ is insensitive to the height of the representative rectangular region. The influence of air and nearby pixels with trivial particle content is then removed through a threshold, which is lower than the corresponding ϕ_0. Additionally, the local interfacial deformation σ_{loc} is obtained by characterizing the local standard deviation between the neighboring plumes [Fig. 9(b)].

A comprehensive comparison between interacting and noninteracting plumes reveals distinct quantitative differences in their spatial arrangement and morphological evolution. Interacting plumes consistently originate at smaller initial separations (S) than their noninteracting counterparts, implying that proximity at formation plays a critical role in governing plume-plume interactions [see Fig. 9(c)]. This close spacing results in a higher time-averaged interplume concentration $\langle\bar{\phi}_{ip}\rangle$, as evident in Fig. 9(a). Furthermore, the local interfacial deformation is markedly smaller for interacting plumes [Fig. 9(b)]. This result is counterintuitive at first glance: although the overall interfacial deformation is highest in the regimes where interacting plumes are most prevalent [i.e., the merging plumes and plume shedding regimes; see Fig. 7(a)], the local deformation between interacting plumes is invariably lower. In the plume shedding regime, σ_{loc}/b for interacting plumes is an order of magnitude smaller than that of noninteracting ones.

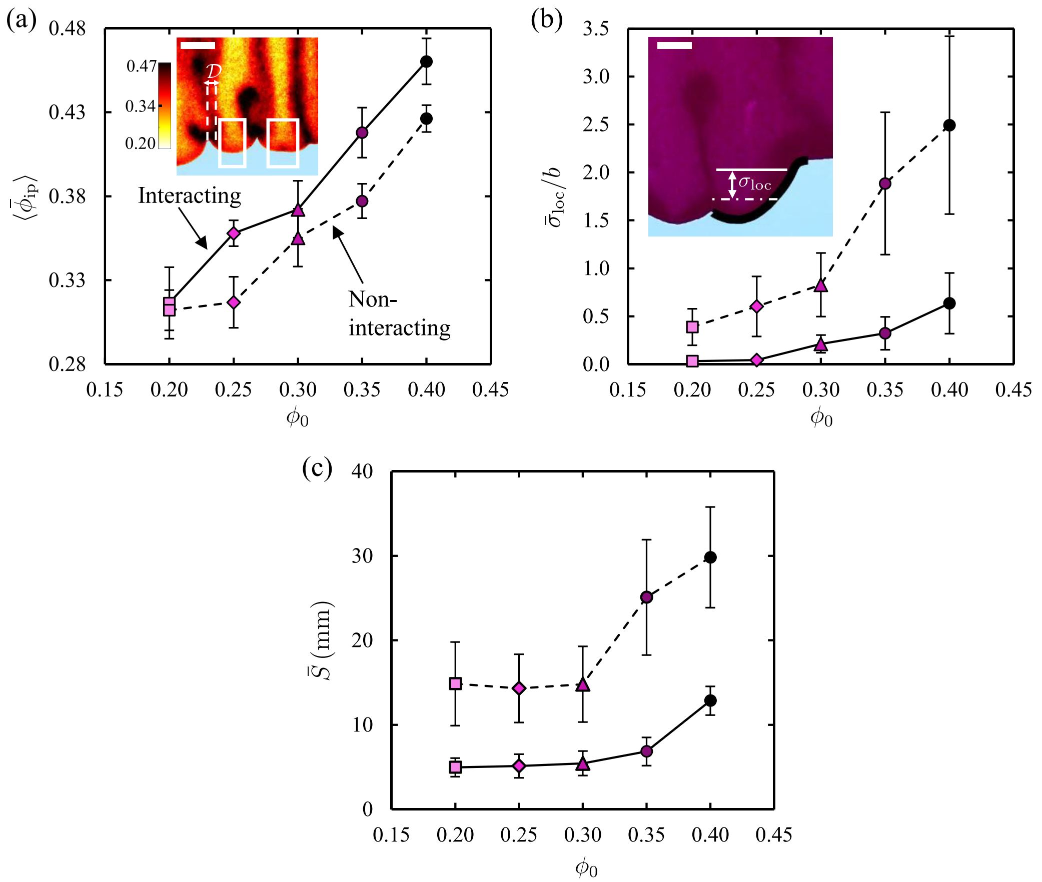

FIG. 9. Comparison of the time-averaged interplume concentration, $\langle\bar{\phi}_{\rm ip}\rangle$, the time-averaged dimensionless local interfacial deformation, $\bar{\sigma}_{\rm loc}/b$, and the time-averaged initial plume-plume spacing, $\bar{S}$, as functions of ϕ_0 for interacting (solid lines) and noninteracting plumes (dashed lines). (a) $\langle\bar{\phi}_{\rm ip}\rangle$ versus ϕ_0. The inset clarifies the region used to determine $\bar{\phi}_{\rm ip}$, where an offset distance $\mathcal{D}$ from the plume tips excludes the plume cores from the calculation. (b) $\bar{\sigma}_{\rm loc}/b$ versus ϕ_0. The inset defines the parameters associated with local interfacial deformation: the white dash-dotted line represents the local mean interface position between two successive plume tips, while the white solid line marks one local standard deviation from this mean. (c) $\bar{S}$ versus ϕ_0. Here, S is defined as the horizontal distance between neighboring plume tips. Scale bars in (a) and (b) indicate 1 cm.

To more closely examine these results, we consider how the local interfacial deformation $\sigma_{\rm loc}/b$ and interplume concentration $\bar{\phi}_{\rm ip}$ evolve over time for a pair of interacting plumes in Fig. 10. As shown in Fig. 10(a), the local interfacial deformation progressively decreases over the course of interaction and eventually approaches zero at the moment of merging, which explains why $\bar{\sigma}_{\rm loc}/b$ may be lower for interacting plumes than for noninteracting ones. Simultaneously, the plume tips are gradually drawn toward each other during interaction. The final merged tip forms at a location approximately midway between the initial positions of the interacting plumes, as quantified in the inset of Fig. 10(a). Meanwhile, the interplume concentration $\bar{\phi}_{\rm ip}$ steadily rises throughout the interaction [Fig. 10(b)]. The elevated concentration arises because particles preferentially accumulate at concave tips (see Sec. IV B); when two tips converge, their surrounding "feeding" zones overlap, leading to enhanced particle accretion in the interplume region.

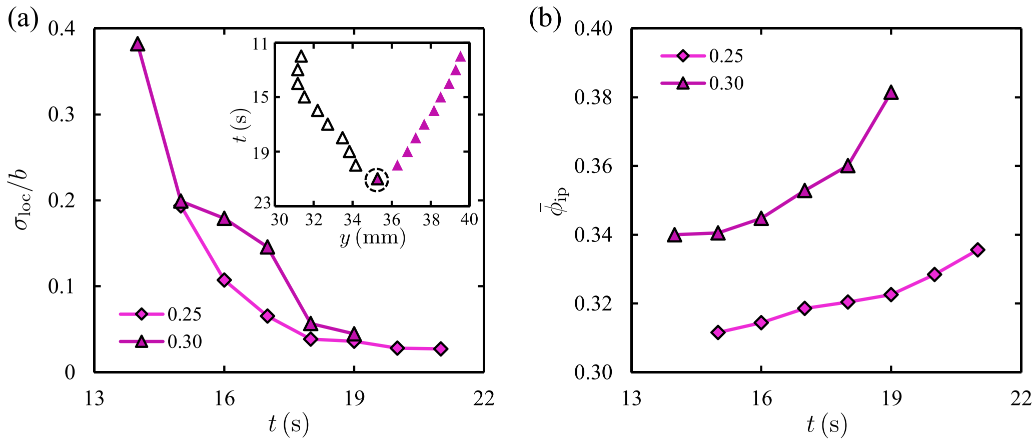

FIG. 10. Time variation of normalized local interfacial deformation σ_{loc}/b and interplume concentrtion $\bar{\phi}_{\mathrm{ip}}$ for two interacting plumes at $\phi_0 = 0.25$ and 0.30. (a) σ_{loc}/b as a function of time. The inset displays the lateral trajectories of the plume tips for two interacting plumes at $\phi_0 = 0.30$, tracked from the moment the second plume emerges until their eventual merging (marked by a dashed circle). Time progresses downward along the vertical axis. (b) $\bar{\phi}_{\mathrm{ip}}$ as a function of time.

IV. PHYSICAL MECHANISM

In this section, we combine modeling and scaling arguments to rationalize some of our experimental findings. We first elucidate the mechanism of particle accumulation at the suspension-air interface through the suspension balance model. Building on this, we introduce a scaling analysis to describe plume initiation and growth, only relevant for the isolated and merging plumes regimes.

A. Particle migration: Key to pattern formation

The key mechanism underlying pattern formation is shear-induced migration of noncolloidal particles [30], whereby particles move from high-shear toward low-shear zones to minimize particle-particle collisions. In a pressure-driven flow inside a channel, particles move toward the channel centerline by this mechanism, where the velocity is higher. The resulting migration produces a net particle flux Q_{p}, which leads to particle accumulation at the interface, as schematically illustrated in Fig. 11(a). This accumulation is experimentally quantified in Fig. 11(b), which displays $\bar{\phi}$ as a function of the streamwise coordinate x for $\phi_0 = 0.25$. Each data point is acquired by averaging $\bar{\phi}$ over the channel width w at given x. When normalized by the instantaneous mean interface position $\bar{\ell}$, $\bar{\phi}$ profiles reveal a self-similar trend and approximately collapse into a single curve, as previously observed in the radial flow [31].

We divide $\bar{\phi}$ into two regions: (i) Region I ($0 < x < \ell_{\mathrm{I}}$) far upstream from the interface where $\bar{\phi}$ remains approximately uniform, and (ii) Region II ($\ell_{\mathrm{I}} < x < \bar{\ell} = \ell_{\mathrm{I}} + \ell_{\mathrm{II}}$) where $\bar{\phi}$ increases towards the interface. Here, ℓ_{I} and ℓ_{II} correspond to the streamwise lengths of Regions I and II, respectively, where ℓ_{I} is empirically determined by locating the streamwise position at which the gradient of smoothened $\bar{\phi}$ exceeds a prescribed threshold [see Fig. 11(c)]. While $\bar{\phi}\,(x/\bar{\ell})$ is mostly time invariant, the maximum value in $\bar{\phi}$ near the advancing interface is shown to increase over time. Finally, this two region description is not directly applicable to the plume shedding regime, which is not the focus of this section.

To further validate this physical picture, we theoretically model the particle-laden flow in Region I, based on the suspension balance model [36]. As detailed in Appendix E, we compute the particle concentration $\phi\,(z)$ inside the thin gap by assuming a 1D quasi-fully-developed flow, far upstream from the interface. The plots of $\phi\,(z)$ in Fig. 12(a) for varying ϕ_0 indeed reveal larger

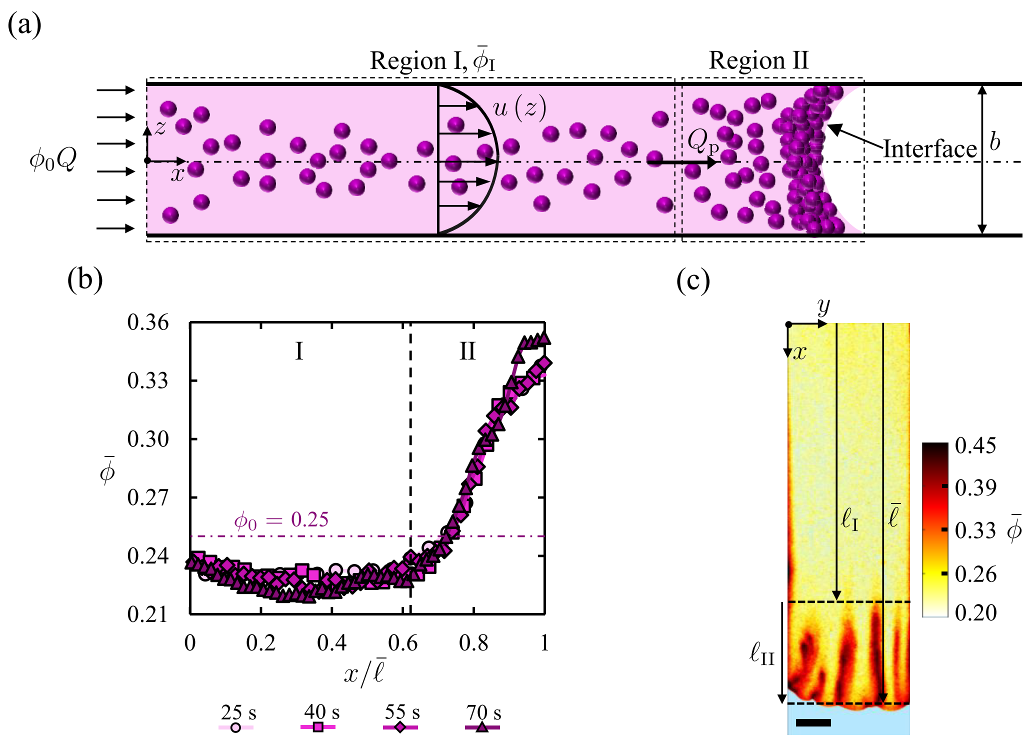

FIG. 11. (a) Schematic side view (z-x plane) of the rectangular Hele-Shaw cell, illustrating how shear-induced migration drives particles toward the mid-plane ($z = 0$), creating a net particle flux ($Q_{\rm p}$) toward the interface. This results in a less concentrated upstream zone (Region I) with an approximately uniform concentration and a more concentrated zone near the interface (Region II). (b) Streamwise profiles of $\bar{\phi}$ as a function of $x/\bar{\ell}$ at different times for $\phi_0 = 0.25$. Upon normalization by $\bar{\ell}$, the profiles collapse onto a single self-similar curve. For this experiment, the transition from Region I to Region II occurs at $x/\bar{\ell} \approx 0.6$, remaining nearly invariant over time. (c) Corresponding $\bar{\phi}$ field at $t = 55$ s, highlighting the mean interface position $\bar{\ell}$, the length of Region I ($\ell_{\rm I}$), and the length of Region II ($\ell_{\rm II}$).

ϕ at the midplane ($z = 0$) relative to the wall ($z = b/2$), showing the effects of shear-induced migration. Figure 12(b) compares the theoretically calculated depth-averaged concentration, obtained by integrating $\phi(z)$ across the gap, with the experimentally determined values of $\bar{\phi}_{\rm I}$, the mean concentration of Region I. The theoretical and experimental results exhibit strong agreement, with an average relative error of only 5.1%.

Since $\bar{\phi}_{\rm I}$ is consistently lower than ϕ_0 as seen below the dashed line of unit slope in Fig. 12(b), a net particle flux $Q_{\rm p}$ is generated from Region I into Region II:

$$Q_{\rm p} = w \int_{-b/2}^{b/2} \phi(z)(u(z) - U)dz, \tag{5}$$

where $u(z)$ is the velocity profile in Region I, and $U \approx Q/bw$ is the speed of the downstream boundary. With $\bar{\phi}_{\rm I} = 1/b \int_{-b/2}^{b/2} \phi(z)dz$ and $Q\phi_0 = \int_{-b/2}^{b/2} u\phi(z)dz$ based on mass conservation (see Appendix E), the particle flux reduces to

$$Q_{\rm p} = (\phi_0 - \bar{\phi}_{\rm I})Q, \tag{6}$$

which is indeed positive as long as $\bar{\phi}_{\rm I} < \phi_0$. We verify that $\phi_0 - \bar{\phi}_{\rm I} > 0$ as a function of ϕ_0 in Fig. 12(c), which shows the same qualitative trend for both theory and experiments. The model

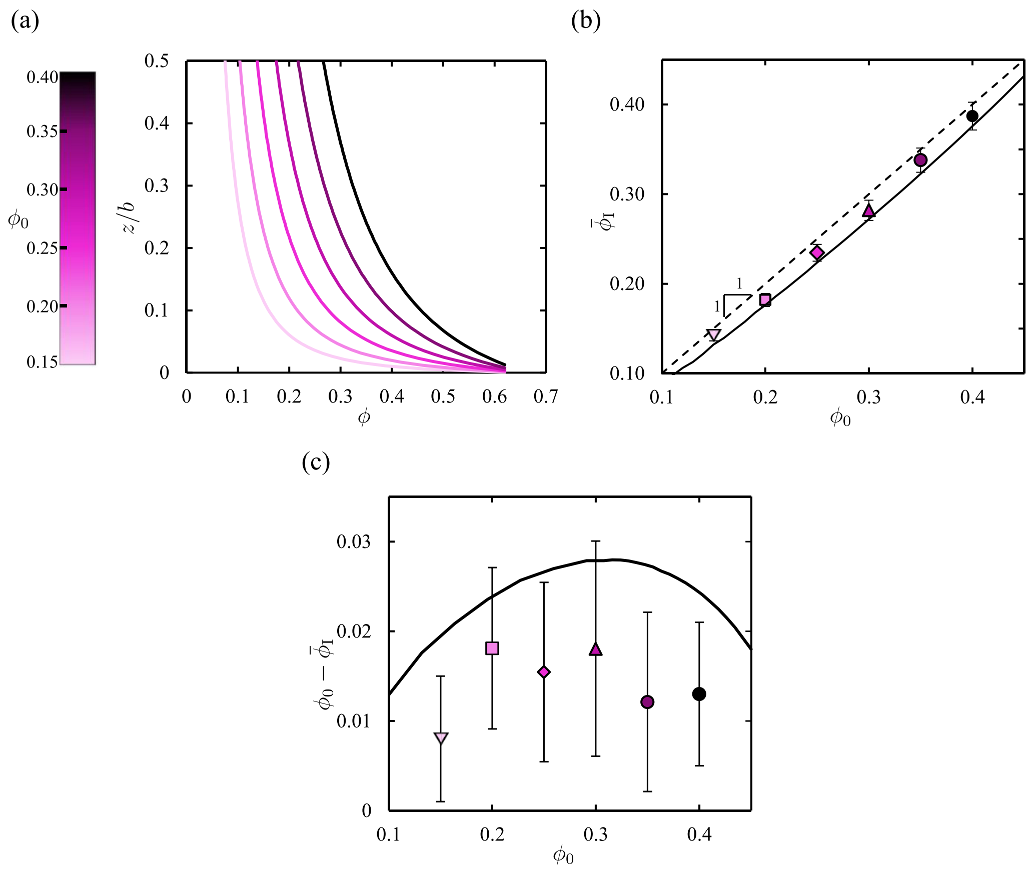

FIG. 12. (a) Particle distribution profiles for varying ϕ_0, where shear-induced migration focuses particles near the centerline ($z = 0$). (b) Comparison of the mean concentration in Region I, $\bar{\phi}_{\mathrm{I}}$, versus ϕ_0 between theory (solid line) and experiments (filled symbols). The dashed line represents the line of slope one. (c) Difference between ϕ_0 and $\bar{\phi}_{\mathrm{I}}$ as a function of ϕ_0, showing both theoretical predictions (solid line) and experimental results (filled symbols), with $\bar{\phi}_{\mathrm{I}} < \phi_0$ in all cases.

underpredicts $\bar{\phi}_{\mathrm{I}}$, resulting in slightly larger values of $\phi_0 - \bar{\phi}_{\mathrm{I}}$ compared to the experimental measurements.

B. From particle flux to plume formation

Having rationalized a nonzero particle flux towards the interface, we now discuss how nascent particle clusters introduced in Sec. III B develop into plumes and give rise to interfacial fingers. As particles continuously accumulate on the interface, any perturbations in the particle enrichment can cause spatial variations in the effective viscosity, which, in turn, leads to segments of the interface with higher viscosity lagging behind the advancing front. As a result, the interface develops concave tips, as schematically illustrated in Fig. 13(a). For simplicity, the interface is idealized as a locally concave segment at the plume tip, labeled A, and a radius of curvature δ, while the transverse curvature can be approximated as $-2/b$ with the suspending oil perfectly wetting the glass plates. Thus, we use the Young-Laplace relation [46] to estimate the pressure at the concave tip as

$$p_{\mathrm{A}} \approx p_{\mathrm{air}} - \gamma \left[\frac{1}{\delta} + \frac{2}{b} \right], \tag{7}$$

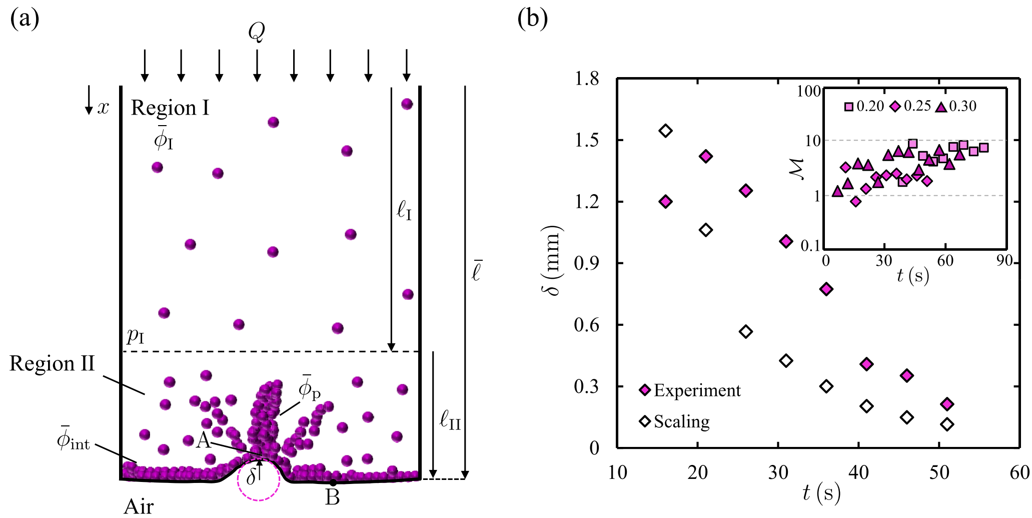

FIG. 13. (a) Schematic of the 1D scaling framework for plume formation. Region I supplies a nearly uniform background suspension flow with mean concentration $\bar{\phi}_{\rm I}$. In Region II, curvature of the suspension-air interface creates local pressure variations: the concave plume tip (A) exhibits a lower pressure than adjacent, weakly curved regions such as B. This reduced pressure redirects streamlines toward the tip, funneling particles into it, thereby establishing the tip as a particle sink. (b) Comparison of experimentally measured (filled symbols) values of δ with predictions from Eq. (10) (open symbols) for a representative plume at $\phi_0 = 0.25$. The inset shows the time evolution of the dimensionless parameter $\mathcal{M}$, defined as the ratio of the experimentally determined tip radius of curvature to that obtained from Eq. (10), for representative plumes across different ϕ_0. The vertical axis is shown on a logarithmic scale.

where $p_{\rm air}$ is the constant pressure in the air phase. Note that, since the particles are fully wetted by the oil phase and likely do not adsorb on the oil-air interface, they are not expected to modify the interfacial energy. Accordingly, the interfacial tension γ is taken to be that of the pure oil-air interface, independent of particle concentration. As $\delta > 0$, $p_{\rm A}$ is lower than that at the nearly flat portions of the interface (e.g., point B), where $p_{\rm B} \approx p_{\rm air} - 2\gamma/b$.

This localized reduced pressure establishes an enhanced pressure gradient directed toward the tip. As the upstream flow in Region I continuously supplies a net particle flux into Region II, this results in more particles flowing towards the tip relative to undeformed, neighboring regions. Through this sequence of events (i.e., particle accumulation, tip formation, and particle focusing), a nascent cluster evolves into a mature plume. A similar focusing process also governs the behavior of plumes when they interact. In the case of interacting plumes, their tips simultaneously draw particles from the upstream zone (Region I) while moving closer to each other laterally [see the inset of Fig. 10(a)]. As they approach, the particle-feeding fluxes associated with each tip increasingly overlap within the narrowing region between them, causing interacting plumes to receive more particles than their noninteracting counterparts. As a result, the interplume concentration $\bar{\phi}_{\rm ip}$ becomes markedly higher for interacting plumes than for noninteracting ones, consistent with Fig. 9(a).

So far, we have established that concave tips act as particle sinks, thereby augmenting the plume concentration. This is consistent with the temporal increase in $\bar{\phi}_{\rm p}$ observed in the isolated and merging plumes regimes [see Fig. 7(b)]. At the same time, as the tip becomes increasingly particle rich and lags further behind the surrounding interface, the local pressure gradient must increase due to decreasing δ. A natural question, then, is how the interface avoids unbounded deformation. Left unchecked, continuous particle focusing toward the tip would continuously decelerate the tip and drive δ to progressively smaller values, ultimately leading to cusp formation.

The answer lies in the dual role of the pressure gradient. On one hand, the pressure gradient diverts particles toward the tip, allowing the upstream suspension (Region I) to feed the tip more effectively. Via Darcy's law [Eq. (2)], this enhanced gradient increases the local tip velocity. At certain instants, the tip velocity may even exceed the interface velocity U, momentarily relaxing the interface and bringing the pressure gradient back down. This, in turn, decreases the tip speed and resets the whole process. If the tip slows down to be below U, it would locally deform the interface more and increase the pressure gradient, causing the tip to speed up. Hence, after the initial transient period, these coupled processes form a feedback loop ensuring that the plume tips on average must move at U. In other words, the effects of enhanced viscosity and increased pressure gradient due to the tip formation must cancel each other out in the steady state, such that the plume tips on average move at U. This also explains why the interfacial deformation does not grow over time in the isolated plumes regime. Note that the acceleration and deceleration of plume tips tend to fluctuate irregularly in time, with typical timescales on the order of $O(1\text{ s})$ in the experiments.

While the qualitative mechanism is now clear, a quantitative connection between the pressure drop at the tip, tip curvature, and the viscosity contrast remains to be established. Although we acknowledge that the particles move faster than the mixture in Region I due to shear-induced migration, particles are assumed to move with the local flow near the interface, as previously shown in [35]. Hence, in Region II, we approximate the flow as a 1D Darcy flow [Eq. (2)] and estimate the pressure gradient near the interface based on p_{I} for simplicity. As illustrated in Fig. 13(a), p_{I} refers to the uniform gauge pressure at the downstream boundary of Region I, where the flow remains unaffected by interfacial deformation. When combined with Eq. (7), the resulting pressure gradient driving enhanced particle flux toward the tip A is approximated as $[p_{\mathrm{I}} + \gamma(2/b + 1/\delta)]/\ell_{\mathrm{II}}$ based on $\delta \ll \ell_{\mathrm{II}}$, which is larger than that toward B, i.e., $(p_{\mathrm{I}} + 2\gamma/b)/\ell_{\mathrm{II}}$. Substituting the expression for the pressure gradient into Darcy's law, we obtain the following relation for the tip velocity U_{A}:

$$U_{\mathrm{A}} \approx \frac{b^2}{12\mu(\bar{\phi}_{\mathrm{p}})} \frac{p_{\mathrm{I}} + \gamma(2/b + 1/\delta)}{\ell_{\mathrm{II}}}, \tag{8}$$

where $\mu(\bar{\phi}_{\mathrm{p}})$ is the plume viscosity. Similarly, the interfacial velocity at flatter portions of the interface is

$$U \approx \frac{Q}{bw} \approx \frac{b^2}{12\mu(\bar{\phi}_{\mathrm{int}})} \frac{p_{\mathrm{I}} + 2\gamma/b}{\ell_{\mathrm{II}}}, \tag{9}$$

where $\bar{\phi}_{\mathrm{int}}$ denotes the mean concentration at the interface. Note that p_{I} can be obtained from Eq. (9), showing its dependence on the flow rate, channel geometries, and the time-dependent suspension length. Based on the aforementioned feedback mechanism, we set $U_{\mathrm{A}} \approx U$ and arrive at the following scaling for δ:

$$\delta \propto \frac{\mu(\bar{\phi}_{\mathrm{int}})}{\mu(\bar{\phi}_{\mathrm{p}}) - \mu(\bar{\phi}_{\mathrm{int}})} \left[\frac{\gamma}{p_{\mathrm{I}} + 2\gamma/b}\right]. \tag{10}$$

Equation (10) implies that the upstream pressure, interfacial tension, and local particle concentrations collectively determine the radius of curvature.

To assess the validity of Eq. (10), we experimentally measure δ from the fitted curve to the interface and compare its values with the corresponding scaling predictions. Figure 13(b) illustrates this comparison for a representative plume at $\phi_0 = 0.25$, where Eq. (10) accurately captures both the correct order of magnitude and the temporal evolution of δ. It is worth mentioning that the increase in δ at $t = 21$ s arises from a transient acceleration of the tip, which momentarily increases the radius of curvature. We further examine the robustness of the scaling across distinct values of ϕ_0 by defining $\mathcal{M}$ as the ratio of the experimentally measured tip radius of curvature to the value predicted by the scaling. As shown in the inset of Fig. 13(b), $\mathcal{M}$ consistently falls between $O(1)$ and $O(10)$. This collapse indicates that the simple scaling in Eq. (10) also captures the correct functional dependence of δ across the range of initial particle concentrations considered.

V. CONCLUSION

In this work, we experimentally investigate the spontaneous formation of patterns in particle-induced viscous fingering (PIVF) when a noncolloidal oil suspension displaces air inside a rectangular Hele-Shaw cell. Across our experiments with varying ϕ_0, interfacial deformation and particle plumes emerge as the dominant patterns, whose evolution can be classified into four regimes: stable, isolated plumes, merging plumes, and plume shedding. The latter two regimes are, to our knowledge, newly identified in this work. We quantify both interfacial deformation and plume concentration to uncover a strong coupling between the two.

To help explain this coupling, we first rationalize the net flux of particles Q_p toward the advancing fluid-fluid interface due to the shear-induced migration of noncolloidal particles. As particles accumulate on the interface, particle clustering near the interface locally increases the effective viscosity, slowing down those segments of the front and deforming the interface. Then, the deformed parts of the interface, or concave tips, experience a reduced pressure relative to the surrounding interface, which focuses more particles toward the tip and initiates plume growth. The same mechanism also governs plume-plume interactions. Scaling arguments further reveal that the tip radius of curvature is governed by the interplay between upstream pressure, local particle concentrations, and interfacial tension, in reasonable agreement with the experiments. Finally, we suggest a feedback mechanism rooted in the dual role of the pressure gradient: while it focuses particles into the tip and amplifies viscosity contrasts, it also intermittently relaxes interfacial deformation, preventing cusp formation and stagnation. This feedback loop maintains plume growth, while the interfacial deformation remains bounded in the isolated plumes regime.

This study has illuminated key aspects of pattern formation in PIVF and yet leaves many more to be explored. While our present analysis explains the coupling between the plume tip and interfacial fingers, it fails to rationalize the mechanism of wavelength selection, which will involve stability analysis in rectilinear geometry [35]. Furthermore, the plume shedding regime is observed for dense suspensions that may be approaching a shear-jamming limit. We plan to investigate the onset of the plume shedding regime and the dynamics of detached particle islands for varying particle sizes and channel geometries. In particular, exploring the connection between our observation and other similar shedding events [42,43] would enhance our current understanding greatly. In addition to focusing on the plume shedding regime, extending the experiments to viscous immiscible defending fluids provides a complementary pathway to probe how the viscosity ratio and interfacial tension between the invading suspension and defending fluid can either amplify or suppress the emergence of complex interfacial patterns. Our preliminary experiments with immiscible water-glycerol mixtures show delayed plume formation with reduced interfacial deformations, which points to the nontrivial effects of the fluid properties on the particle-induced pattern generation.

ACKNOWLEDGMENT

This work was partly supported by the National Science Foundation (Grants No. DMR-2003706 and No. EAR-2100493).

DATA AVAILABILITY

The data that support the findings of this article are not publicly available upon publication because it is not technically feasible and/or the cost of preparing, depositing, and hosting the data would be prohibitive within the terms of this research project. The data are available from the authors upon reasonable request.

TABLE I. Influence of oil viscosity μ_1, suspension flow rate Q, and channel width w on pattern formation characteristics for $\phi_0 = 0.25$.

No.	μ_1 (Pa s)	Q (ml/min)	w (mm)	$\bar{n}_\mathrm{p}$	$\bar{\lambda}$ (mm)	$\bar{\sigma}/b$	$\langle\bar{\phi}_\mathrm{p}\rangle$
1	0.048	25	70	4.5 ± 1.1	14.6 ± 3.3	1.6 ± 0.44	0.41 ± 0.017
2	0.096	25	70	4.2 ± 0.81	15.2 ± 3.7	1.6 ± 0.32	0.42 ± 0.030
3	0.048	50	70	4.5 ± 0.78	14.2 ± 2.5	1.9 ± 0.15	0.41 ± 0.021
4	0.048	25	98	5.65 ± 1.1	14.9 ± 2.0	1.4 ± 0.35	0.43 ± 0.032

APPENDIX A: EFFECTS OF OIL VISCOSITY, SUSPENSION FLOW RATE, AND CHANNEL WIDTH

To examine the impact of suspension flow rate, channel width, and oil viscosity, we consider a reference experiment ($\phi_0 = 0.25$, $\mu_1 = 0.048$ Pa s, $Q = 25$ ml/min, and $w = 70$ mm) and vary one control parameter at a time, while keeping ϕ_0 fixed. Specifically, we independently vary (i) the oil viscosity to $\mu_1 = 0.096$ Pa s, (ii) the suspension flow rate to $Q = 50$ ml/min, and (iii) the channel width to $w = 98$ mm, with all other parameters held constant. Table I summarizes the resulting pattern formation characteristics for these cases. Here, $\bar{\lambda}$, $\bar{\sigma}/b$, $\langle\bar{\phi}_\mathrm{p}\rangle$, and $\bar{n}_\mathrm{p}$ denote the time-averaged instability wavelength, normalized interfacial deformation, plume concentration, and number of plumes, respectively.

At higher suspension flow rates, interfacial deformation generally increases, and plumes emerge earlier compared to the reference experiment. This behavior is consistent with the shear-induced migration (Sec. IV A), which scales as $\dot{\gamma} d^2$, where $\dot{\gamma}$ is the shear rate [47]. As Q increases, the shear rate rises, leading to faster particle accumulation at the interface and an earlier onset of plume formation. In contrast, no deviation from the reference experiment is observed when the viscosity of the suspending oil is varied. This can be understood from Eq. (10), where δ depends on the ratio of suspension viscosities evaluated at different local particle concentrations, causing the influence of μ_1 to cancel out [see Eq. (3)]. Consequently, δ, and hence the interfacial deformation, are largely independent of μ_1. In addition, increasing the channel width leads to a higher number of plumes, while the instability wavelength remains approximately constant. The total number of merging events also increases with w, which is expected since a wider channel accommodates more plumes at an approximately constant wavelength, thereby augmenting the number of interacting plume pairs.

Overall, altering Q, μ_1, or w does not trigger transitions between pattern formation regimes, with all four cases remaining within the same regime. We emphasize that these observations are valid within the range of parameters considered. For instance, our experiments indicate that at sufficiently low flow rates, the interfacial velocity may fall below the particle settling speed, suppressing particle flux toward the interface and preventing plume formation.

APPENDIX B: CALIBRATION

To calibrate the measurements of $\bar{\phi}$, suspensions of known concentration (ranging from 0.10 to 0.50) are prepared. In lieu of injecting the suspension into the Hele-Shaw cell, we place the suspension between the plates, with the gap thickness fixed equal to that employed in the experiments. To ensure consistency, the calibration measurements are performed using the same glass plates, lighting conditions, and camera settings as in the main runs. The suspensions are then imaged under these conditions, yielding a calibration curve that relates image intensity to particle concentration. Since the data are extracted after background subtraction, the calibration curve is applicable across the entire imaging area for all experiments. The resulting $\bar{\phi}$ values are further corrected using a time-dependent correction factor, $c(t)$, ranging from 1.0 to 1.2, obtained

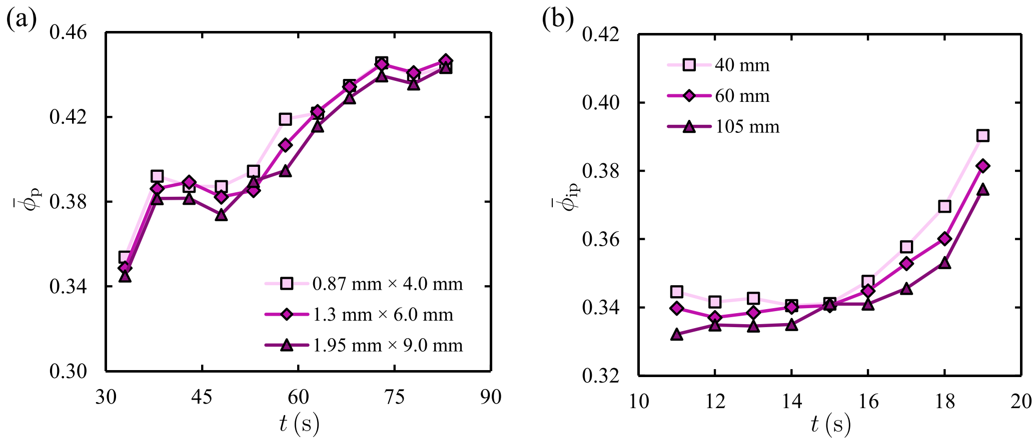

FIG. 14. (a) $\bar{\phi}_p$ as a function of time for a representative plume at $\phi_0 = 0.20$ evaluated by three distinct sizes of rectangular regions defined above the tip. (b) $\bar{\phi}_{ip}$ as a function of time for two interacting plumes at $\phi_0 = 0.30$, evaluated for different heights of the rectangular region defined between two neighboring plumes.

by enforcing particle conservation:

$$c\,(t) = \frac{\phi_0 \iiint dV}{\iiint \bar{\phi}\, dV}, \tag{B1}$$

where the numerator represents the theoretical particle volume within the cell, while the denominator corresponds to the experimentally measured particle volume.

APPENDIX C: SENSITIVITY OF $\bar{\phi}_p$ AND $\bar{\phi}_{ip}$ TO REPRESENTATIVE REGION SIZE

To examine the effect of the size of the window defined above the plume tip on the depth-averaged plume concentration $\bar{\phi}_p$, we measure the plume concentration over time at $\phi_0 = 0.20$ by considering three window dimensions: 0.87 mm × 4.0 mm, 1.3 mm × 6.0 mm, and 1.95 mm × 9.0 mm [Fig. 14(a)]. The sensitivity analysis indicates that the maximum and mean relative error in $\bar{\phi}_p$ between the fine and medium windows are only 1.05% and 3.0%, respectively. Similarly, the maximum and mean relative differences between the medium and coarse windows are 1.49% and 3.0%, respectively. These small variations indicate that the measured plume concentration is effectively independent of the window size, consistent with the relatively uniform concentration from tip to tail.

Likewise, we explore the time evolution of $\bar{\phi}_{ip}$ for two interacting plumes at $\phi_0 = 0.30$ by considering window heights of 40, 60, and 90 mm [Fig. 14(b)]. The mean and maximum relative errors between the medium and fine window sizes are 1.28% and 2.64%, respectively. Corresponding values between the medium and coarse window sizes are 1.34% and 2.23%. These results indicate that the height of the rectangular region has a negligible influence on the outcomes.

APPENDIX D: TEMPORAL TREND OF $\bar{\phi}_p$ FOR DIFFERENT PLUMES AT THE SAME REGIME

Figure 15 illustrates the time evolution of $\bar{\phi}_p$ at $\phi_0 = 0.30$ for distinct plumes. Within the same regime, both the overall trend and the range of variation of $\bar{\phi}_p\,(t)$ are consistent across different plumes and appear independent of the specific plume considered, with only minor fluctuations in magnitude.

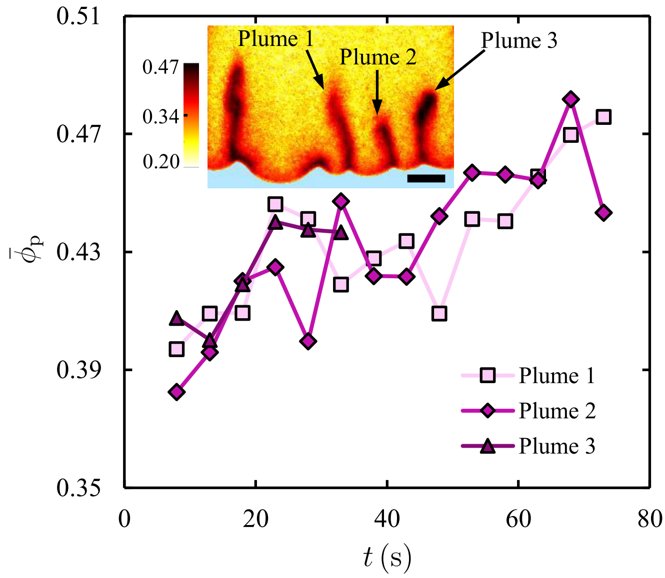

FIG. 15. Time variation of $\bar{\phi}_{\rm p}(t)$ for different plumes across the merging plumes regime ($\phi_0 = 0.30$). Plume 3 has a shorter lifetime as it collides with the wall and is annihilated after $t = 40$ s. Scale bar denotes 1 cm.

APPENDIX E: SUSPENSION BALANCE MODEL

Following the work of [32], we use the suspension balance model [36,37] to model the flow in Region I. Assuming the inertialess (Stokes) regime and a neutrally buoyant suspension in which both the suspending fluid and the particles are incompressible, the conservation of mass and momentum for the bulk suspension can be expressed as

$$\nabla \cdot \mathbf{u} = 0, \tag{E1a}$$

$$\nabla \cdot \boldsymbol{\Sigma} = 0, \tag{E1b}$$

where $\mathbf{u}$ denotes the suspension velocity, while $\boldsymbol{\Sigma}$ symbolizes the suspension stress tensor. Likewise, the particle phase is governed by

$$\frac{\partial \phi}{\partial t} + \nabla \cdot (\phi \mathbf{u}^{\rm p}) = 0, \tag{E2a}$$

$$\nabla \cdot \boldsymbol{\Sigma}^{\rm p} + \mathbf{F} = 0, \tag{E2b}$$

where $\mathbf{u}^{\rm p}$ and $\boldsymbol{\Sigma}^{\rm p}$ are the velocity and stress tensor of the particle phase, respectively, and $\mathbf{F}$ denotes the interphase drag force that depends on the relative velocity between the bulk suspension and the particle phases [48]:

$$\mathbf{F} = -18\frac{\mu_1}{d^2}\frac{\phi}{(1-\phi)^5}(\mathbf{u}^{\rm p} - \mathbf{u}), \tag{E3}$$

where μ_1 is the suspending fluid (oil) viscosity. Utilizing the continuity (E1a), the particle transport relation (E2a) can be written as

$$\frac{\partial \phi}{\partial t} + \mathbf{u} \cdot \nabla \phi = -\nabla \cdot [\phi(\mathbf{u}^{\rm p} - \mathbf{u})]. \tag{E4}$$

The coupling between the suspension and particle phases is captured through the constitutive relations for the stress tensors

$$\mathbf{\Sigma} = -p\mathbf{I} + \mathbf{\Sigma}^{\mathrm{p}} + 2\mu_1\mathbf{E}, \tag{E5a}$$

$$\mathbf{\Sigma}^{\mathrm{p}} = \mathbf{\Sigma}^{\mathrm{p}}_{\mathrm{n}} + 2(\mu_{\mathrm{s}}(\phi) - \mu_1)\mathbf{E}, \tag{E5b}$$

where $\mathbf{I}$, p, and μ_{s} represent the identity matrix, bulk suspension pressure, and the effective shear viscosity of the bulk suspension [e.g., Eq. (3)]; $\mathbf{E}$ is the strain rate tensor, while $\mathbf{\Sigma}^{\mathrm{p}}_{\mathrm{n}} \propto \mu_{\mathrm{n}}\dot{\gamma}$ is the particle normal stress tensor [37]. Here, $\dot{\gamma} = (2\mathbf{E} : \mathbf{E})^{1/2}$ stands for the shear rate, and μ_{n} denotes the effective normal viscosity of the bulk suspension [37]

$$\frac{\mu_{\mathrm{n}}(\phi)}{\mu_1} = 0.75\left(\frac{\phi}{\phi_{\mathrm{m}}}\right)^2\left(1 - \frac{\phi}{\phi_{\mathrm{m}}}\right)^{-2}. \tag{E6}$$

To simplify the governing equations, the parameters are nondimensionalized as follows:

$$x^* = \frac{x}{L_0}, \quad z^* = \frac{z}{b}, \quad \mu^*_{\mathrm{s/n}} = \frac{\mu_{\mathrm{s/n}}}{\mu_1}, \quad p^* = \frac{p}{\mu_1 U L_0/b^2},$$
$$u^* = \frac{u}{U}, \quad w^* = \frac{w}{\epsilon U}, \quad \mathbf{\Sigma}^{p*} = \frac{\mathbf{\Sigma}^p}{\mu_1 U/b}, \quad t^* = \frac{t}{L_0/U}, \tag{E7}$$

where $L_0 \sim O(10^{-1}\ \mathrm{m})$ is the characteristic axial length and $b \sim O(10^{-3}\ \mathrm{m})$ is the Hele-Shaw gap thickness. As $\epsilon \equiv b/L_0 \ll 1$ based on the experimental parameters, we employ the lubrication approximations and further assume that the timescale of particle migration is much shorter than that of the particle advection in the axial flow, which reduces the bulk suspension momentum equation to

$$\frac{\partial p}{\partial x} = \frac{\partial}{\partial z}\left[\mu_s(\phi)\frac{\partial u}{\partial z}\right], \tag{E8a}$$

$$\frac{\partial p}{\partial z} = 0. \tag{E8b}$$

Note that, unless otherwise stated, all dependent and independent variables are expressed in dimensionless form, with the asterisk notation omitted for brevity.

Subsequently, combining Eqs. (E2b), (E3), and (E5b) and substituting into Eq. (E4) yields the leading-order transport equation

$$\frac{\partial}{\partial z}\left[(1 - \phi^5)\frac{\partial}{\partial z}[\lambda_2\mu_{\mathrm{n}}(\phi)\dot{\gamma}]\right] = 0, \tag{E9}$$

where λ_2 is an empirically determined scalar independent of ϕ [49]. The no-flux boundary condition at the walls requires

$$\left.\frac{\partial}{\partial z}(\lambda_2\mu_{\mathrm{n}}(\phi)\dot{\gamma})\right|_{z=\pm 1/2} = 0. \tag{E10}$$

Integrating Eq. (E9) and imposing the boundary condition (E10) gives

$$\mu_{\mathrm{n}}(\phi)\dot{\gamma} = \text{constant}. \tag{E11}$$

Considering $\partial_z u\,(z = 0) = 0$ and integrating Eqs. (E8a) with respect to z yields

$$\mu_s(\phi)\frac{\partial u}{\partial z} = \frac{\partial p}{\partial x}z. \tag{E12}$$

Accordingly, the shear rate can be rewritten as

$$\dot{\gamma} = \frac{z}{\mu_s(\phi)}\left|\frac{\partial p}{\partial x}\right|. \tag{E13}$$

Afterward, incorporating Eq. (E13) into Eq. (E11) leads to

$$\frac{\mu_s(\phi(z))}{\mu_n(\phi(z))} = C_0 z, \tag{E14}$$

where C_0 is a constant. Introducing Eqs. (3) and (E6) into Eq. (E14) results in the following explicit expression for $\phi\,(z)$:

$$\phi\,(z) = \phi_m[1 - 1.25\phi_m + 0.5\sqrt{(2.5\phi_m)^2 - 4(0.1 - 0.75C_0 z)}]^{-1}. \tag{E15}$$

The suspension velocity is then acquired by integrating Eq. (E12) and imposing the no-slip boundary condition at $z = \pm 1/2$:

$$u\,(z) = \frac{\partial p}{\partial x}\int_z^{1/2} \frac{\tilde{z}}{\mu_s(\phi\,(\tilde{z}))} d\tilde{z}. \tag{E16}$$

The depth-averaged velocity $\bar{u}$ is subsequently obtained by integrating Eq. (E16) across the gap, and C_0 is determined by satisfying conservation of mass: $\bar{u}\phi_0 = \int_{-1/2}^{1/2} u\phi\,(z)dz$.

---

[1] F. Gallaire and P.-T. Brun, Fluid dynamic instabilities: Theory and application to pattern forming in complex media, Philos. Trans. R. Soc. A **375**, 20160155 (2017).
[2] Q. Zhang, S. Zhou, R. Zhang, and I. Bischofberger, Dendritic patterns from shear-enhanced anisotropy in nematic liquid crystals, Sci. Adv. **9**, eabq6820 (2023).
[3] A. Perazzo, G. Tomaiuolo, V. Preziosi, and S. Guido, Emulsions in porous media: From single droplet behavior to applications for oil recovery, Adv. Colloid Interface Sci. **256**, 305 (2018).
[4] M. Haugen, O. P. Folkvord, T. Veien, M. A. Fernø, and B. Brattekås, Multi-scale dissolution dynamics for carbon sequestration in carbonate rock samples, Gas Sci. Eng. **119**, 205139 (2023).
[5] M. Kasischke, S. Hartmann, K. Niermann, M. Smarra, D. Kostyrin, U. Thiele, and E. L. Gurevich, Pattern formation in slot-die coating, Phys. Fluids **35**, 074117 (2023).
[6] S. J. Weinstein and K. J. Ruschak, Coating flows, Annu. Rev. Fluid Mech. **36**, 29 (2004).
[7] B. Zhao, V. S. Sivasankar, S. K. Subudhi, S. Sinha, S. Nikfarjam, T. Woehl, and S. Das, Three-dimensional deposits from drying particle-laden drops, Langmuir **39**, 9773 (2023).
[8] C.-J. Bae and J. W. Halloran, A segregation model study of suspension-based additive manufacturing, J. Eur. Ceram. Soc. **38**, 5160 (2018).
[9] Q. M. Qi and E. S. G. Shaqfeh, Theory to predict particle migration and margination in the pressure-driven channel flow of blood, Phys. Rev. Fluids **2**, 093102 (2017).
[10] S. Konidena, J. Lee, K. A. Reddy, and A. Singh, Particle dynamics and pattern formation in a rotating suspension of positively buoyant particles, Phys. Rev. Fluids **3**, 044301 (2018).
[11] Z. Varga, V. Grenard, S. Pecorario, N. Taberlet, V. Dolique, S. Manneville, T. Divoux, G. H. McKinley, and J. W. Swan, Hydrodynamics control shear-induced pattern formation in attractive suspensions, Proc. Natl. Acad. Sci. USA **116**, 12193 (2019).
[12] P. Brockmann, M. Tvarozek, M. Lausch, and J. Hussong, Pattern formations in particle laden drum flows and Taylor–Couette flows with co-rotating cylinders, Phys. Fluids **35**, 083304 (2023).
[13] L. Baroudi, M. V. Majji, S. Peluso, and J. F. Morris, Taylor–Couette flow of hard-sphere suspensions: overview of current understanding, Philos. Trans. R. Soc. A **381**, 20220125 (2023).
[14] S. Konidena, B. Vowinckel, R. Seto, K. A. Reddy, and A. Singh, Mechanism for axial pattern formation of concentrated suspension in a horizontal rotating cylinder, J. Fluid Mech. **985**, A8 (2024).
[15] M. A. Fardin, T. Divoux, S. Lee, and I. Bischofberger, Pattern formation and instabilities in particulate suspensions, Annu. Rev. Fluid Mech. **58**, 275 (2025).
[16] R. Juanes, Y. Meng, and B. K. Primkulov, Multiphase flow and granular mechanics, Phys. Rev. Fluids **5**, 110516 (2020).

[17] B. Sandnes, H. A. Knudsen, K. J. Måløy, and E. G. Flekkøy, Labyrinth patterns in confined granular-fluid systems, Phys. Rev. Lett. **99**, 038001 (2007).
[18] B. Sandnes, E. G. Flekkøy, and K. J. Måløy, Stick slip displacement of confined granular mixtures: Bubble expansion, Eur. Phys. J.: Spec. Top. **204**, 19 (2012).
[19] C. Chevalier, A. Lindner, and E. Clément, Destabilization of a Saffman-Taylor fingerlike pattern in a granular suspension, Phys. Rev. Lett. **99**, 174501 (2007).
[20] B. C. Druecke, A. Hooshanginejad, R. Mukherjee, P. Poureslami, and S. Lee, Particle-laden filaments from a draining suspension, Soft Matter **21**, 8479 (2025).
[21] B. Sandnes, E. Flekkøy, H. Knudsen, K. Måløy, and H. See, Patterns and flow in frictional fluid dynamics, Nat. Commun. **2**, 288 (2011).
[22] E. G. Flekkøy, B. Sandnes, and K. J. Måløy, Shape of a frictional fluid finger, Phys. Rev. Fluids **8**, 114302 (2023).
[23] R. Holtzman, M. L. Szulczewski, and R. Juanes, Capillary fracturing in granular media, Phys. Rev. Lett. **108**, 264504 (2012).
[24] D. Zhang, J. M. Campbell, J. A. Eriksen, E. G. Flekkøy, K. J. Måløy, C. W. MacMinn, and B. Sandnes, Frictional fluid instabilities shaped by viscous forces, Nat. Commun. **14**, 3044 (2023).
[25] P. G. Saffman and G. I. Taylor, The penetration of a fluid into a porous medium or Hele-Shaw cell containing a more viscous liquid, Proc. R. Soc. Lond. A **245**, 312 (1958).
[26] G. M. Homsy, Viscous fingering in porous media, Annu. Rev. Fluid Mech. **19**, 271 (1987).
[27] J.-D. Chen, Radial viscous fingering patterns in Hele-Shaw cells, Exp. Fluids **5**, 363 (1987).
[28] H. Tang, W. Grivas, D. Homentcovschi, J. Geer, and T. Singler, Stability considerations associated with the meniscoid particle band at advancing interfaces in Hele-Shaw suspension flows, Phys. Rev. Lett. **85**, 2112 (2000).
[29] A. Ramachandran and D. T. Leighton, Jr., Particle migration in concentrated suspensions undergoing squeeze flow, J. Rheol. **54**, 563 (2010).
[30] D. Leighton and A. Acrivos, The shear-induced migration of particles in concentrated suspensions, J. Fluid Mech. **181**, 415 (1987).
[31] Y. Chen, R. Luo, L. Wang, and S. Lee, Self-similarity in particle accumulation on the advancing meniscus, J. Fluid Mech. **925**, A10 (2021).
[32] F. Xu, J. Kim, and S. Lee, Particle-induced viscous fingering, J. Non-Newtonian Fluid Mech. **238**, 92 (2016), Special issue, Viscoplastic Fluids: From Theory to Application 2015 (VPF6).
[33] J. Kim, F. Xu, and S. Lee, Formation and destabilization of the particle band on the fluid-fluid interface, Phys. Rev. Lett. **118**, 074501 (2017).
[34] F. Xu and S. Lee, The enhancement of viscous fingering with bidisperse particle suspension, J. Fluid Mech. **860**, 487 (2019).
[35] A. Hooshanginejad, B. C. Druecke, and S. Lee, Stability analysis of a particle band on the fluid–fluid interface, J. Fluid Mech. **869**, R2 (2019).
[36] P. R. Nott and J. F. Brady, Pressure-driven flow of suspensions: Simulation and theory, J. Fluid Mech. **275**, 157 (1994).
[37] J. F. Morris and F. Boulay, Curvilinear flows of noncolloidal suspensions: The role of normal stresses, J. Rheol. **43**, 1213 (1999).
[38] See Supplemental Material at http://link.aps.org/supplemental/10.1103/tgvb-bh1n for videos exhibiting different flow regimes, which range from “stable” (movie S1), “isolated plumes” (movie S2), “merging plumes” (movie S3), to “plume shedding” (movie S4), as ϕ_0 is increased.
[39] J. Canny, A computational approach to edge detection, IEEE Trans. Pattern Anal. Mach. Intell. **PAMI-8**, 679 (1986).
[40] R. Luo, Y. Chen, and S. Lee, Particle-induced viscous fingering: Review and outlook, Phys. Rev. Fluids **3**, 110502 (2018).
[41] M. Matsumoto, Vortex shedding of bluff bodies: A review, J. Fluids Struct. **13**, 791 (1999).
[42] H. Z. Ford, G. L. Celora, E. R. Westbrook, M. P. Dalwadi, B. J. Walker, H. Baumann, C. J. Weijer, P. Pearce, and J. R. Chubb, Pattern formation along signaling gradients driven by active droplet behavior of cell swarms, Proc. Natl. Acad. Sci. USA **122**, e2419152122 (2025).

[43] N. Shahsavar, X. Fu, and B. Zhao, Fingering instability during mixing-driven precipitation flow, Transp. Porous Media **151**, 323 (2024).

[44] B. P. Muljadi, M. J. Blunt, A. Q. Raeini, and B. Bijeljic, The impact of porous media heterogeneity on non-Darcy flow behaviour from pore-scale simulation, Adv. Water Resour. **95**, 329 (2016), Special issue, Pore Scale Modeling and Experiments.

[45] J. J. Stickel and R. L. Powell, Fluid mechanics and rheology of dense suspensions, Annu. Rev. Fluid Mech. **37**, 129 (2005).

[46] J. W. McLean and P. G. Saffman, The effect of surface tension on the shape of fingers in a Hele Shaw cell, J. Fluid Mech. **102**, 455 (1981).

[47] B. Snook, J. E. Butler, and E. Guazzelli, Dynamics of shear-induced migration of spherical particles in oscillatory pipe flow, J. Fluid Mech. **786**, 128 (2016).

[48] J. Richardson and W. Zaki, Sedimentation and fluidisation: Part I, Chem. Eng. Res. Des. **75**, S82 (1997).

[49] J. Morris and J. Brady, Pressure-driven flow of a suspension: Buoyancy effects, Int. J. Multiphase Flow **24**, 105 (1998).